



OPEN Microwave resonance detection method for hidden crack depth in rock and cementitious mortar

Chuanjing Ou^{1,2}, Yu Chen^{3,4}, Xindong Zhou⁵, Bin Ma^{1✉}, Hongcai Chen⁶ & Chuanting Ou⁶

Before the rock in engineering projects such as mining, tunnel excavation, steep road construction, and oil and gas extraction undergoes failure, macroscopic and microscopic cracks will appear. The management or utilization of these cracks is inseparable from the application of crack detection technology. Some of these cracks are located below the rock surface and have a certain depth, which hinders the application of standard techniques. Therefore, based on the microwave resonance vibration model and using a low-power microwave source along with an enhanced transmission voltage amplitude, this paper proposes a microwave resonance detection method for the depth of hidden rock cracks. Experimental verification was conducted on cement mortar material samples and granite material samples with different preset internal crack depths. The propagation and reflection characteristics of cement mortar and granite material samples were analyzed, and the detection range of hidden crack depth was assessed. The results show that using this method, both cement mortar and granite samples have real-time detection capabilities at the central frequency of 3.667 GHz microwave magnetic field. The method has a fast response speed, and the relative error of the measurement results is within $\pm 5\%$. The theoretical maximum penetration depth for cement mortar material samples is 83–263 mm, and for granite material samples, it is 8311–83,107 mm. By comparing the actual test results of the cement mortar samples with the theoretical prediction results, it is evident that the microwave resonance crack depth detection device detected a maximum depth of 82 mm, which is consistent with the calculated range. The aforementioned method provides a new means for the detection of cracks below the rock surface.

Keywords Microwave resonance vibration model, Hidden depth, Rock materials, Internal crack, Sensor

In mines, tunnels, hillside roadways, and oil and gas reservoirs, rock failures can occur due to high stress or external disturbances^{1–4}. Cracks, both microscopic and macroscopic, start to appear before the rock fails⁵. Preventive measures should be taken during mining, tunneling, and roadway construction to avoid these cracks⁶. However, in oil and gas extraction, these cracks are used intentionally^{7,8}. In fact, whether it is to avoid these cracks or to utilize them, the application of crack characterization technology is indispensable.

Non-destructive testing (NDT) technology can diagnose rock fractures without damaging the rock structure^{9,10}. Guo et al.¹¹, Shi et al.¹², and Wang et al.¹³ used X-ray computed tomography (CT) technology to analyze the fracturing process of soil-rock mixtures, rock shotcrete composite materials, and shale. Li et al.¹⁴ and Liu et al.¹⁵, on the other hand, conducted nuclear magnetic resonance (NMR) porosity analysis on frost-thawed rocks and micro-weathered tuff. However, X-ray CT devices and NMR devices cannot perform real-time or in-situ testing on samples. Real-time fracture characterization techniques or methods include acoustic emission (AE) monitoring^{16–18}, induced thermography^{19–21}, eddy current testing (ECT)^{22–24}, microwave waveguide detection^{25,26}, ground-penetrating radar (GPR) detection^{27,28}, and electromagnetic radiation detection^{29–33}, among others.

The aforementioned crack characterization techniques mainly focus on identifying surface cracks or detecting the fracture depth of cracks. However, some cracks are located beneath the rock surface and have a certain depth

¹School of Architecture and Transportation Engineering, Guilin University of Electronic Technology, Guilin 541004, China. ²Guangxi Key Laboratory of ITS, Guilin University of Electronic Technology, Guilin 541004, China. ³State Key Laboratory for Tunnel Engineering, Guangzhou 510275, China. ⁴Guangdong Key Laboratory of Marine Civil Engineering, Guangdong Research Center for Underground Space Exploitation Technology, School of Civil Engineering, Sun Yat-sen University, Guangzhou 510275, China. ⁵School of Computer Science and Information Security, Guilin University of Electronic Technology, Guilin 541004, China. ⁶Beihai Product Quality Testing Institute, Beihai 536000, China. ✉email: guidianma@163.com

of burial, which poses a challenge to the use of standard techniques such as thermal imaging technology. By using ultrasonic monitoring to track cracks, or employing AE monitoring technology to locate cracks, we can obtain the depth at which cracks are buried, thereby enriching the information on crack characterization³⁴.

Zhang and colleagues³⁵ studied the rock cracking process through AE technology and P-wave velocity measurements, finding that AE can detect micro-cracks at an early stage, P-wave velocity is sensitive to macro-cracks, and the location of micro-cracks can be determined by AE sensors. Veltmeijer and colleagues' experiments found that in Red Pfaelzer sandstone, ultrasonic waves can detect impending failures 40–70% before the occurrence of the failure, and robustly predict the failures through analytical methods³⁶. Podymova et al.³⁷ proposed an acoustic technique for non-destructive testing of the degree of local microcracks in laboratory mineral samples based on laser-generated ultrasound. Zhang et al.³⁸ conducted uniaxial loading and unloading tests on coal and roof sandstone through ultrasonic monitoring, combined with energy damage analysis and ultrasonic characterization, establishing a quantitative relationship between wave velocity and stress, energy, and damage. Zhang et al.³⁹ developed a novel method capable of creating ultrasonic images in a single measurement by combining the linear and nonlinear properties of concrete, and tested four samples containing different inclusions, analyzing the characteristics of the acoustic nonlinear coefficient as it varies with angle. da Costa et al.⁴⁰ studied the behavior of ultrasonic waves in synthetic rock composed of alternating layers of sand-based (porous and permeable) and acrylic (non-porous) materials. They used transducers of 100 kHz, 500 kHz, and 1 MHz to measure the propagation of P-waves and S-waves, and found that the velocities of P-waves and S-waves in the cracked medium were at least twice those in the uncracked medium, with this difference varying as a function of the number of layers.

Zhou et al.⁴¹ developed the ultra-high-frequency particle impact rock-breaking (UPIRB) technology, which utilizes high-frequency impact stress generated by ultrasonic vibration to effectively promote rock degradation and enhance crushing efficiency. Tao et al.⁴² conducted the first study on the impact of microwave-assisted tunnel boring machine (TBM) cutters on rock fragmentation under initial stress, finding that the fragmentation efficiency increased with the decrease of initial stress and was enhanced with the increase of microwave power. Zhang et al.⁴³ found that microwave heating and water cooling significantly alter the fracture toughness of Cracked Straight Through Brazilian Disc (CSTBD) granite: type I toughness decreases with increasing temperature at low crack angles and increases at high crack angles; type II toughness decreases with increasing temperature at any crack angle.

After a comprehensive analysis of the detection methods used in the aforementioned studies, we understand that when detecting concrete cracks, due to the heterogeneity of concrete materials, the frequency of ultrasonic waves is generally limited to below 100 kHz, although some studies use transducers of 1 MHz for defect measurement. In fact, the frequency range for acoustic wave measurement used to detect the depth of cracks in concrete, cement mortar and rock is typically between 16 and 20 kHz. The acoustic wave method is not as responsive in crack characterization as microwave technology. However, microwave technology is commonly used for crack inspection or depth detection on metal surfaces, and often employs passive source mode testing techniques. In the field of rock engineering, microwave technology for crack characterization is not very common. Additionally, in situations with weak signals, the electromagnetic non-destructive testing technology in passive source mode may lead to the effective signal being obscured by background noise, thereby increasing the relative error of the test results.

To quantitatively detect the depth of hidden cracks in rocks, this study, based on the microwave resonance vibration model proposed by Ou et al.⁴⁴, achieves the quantitative detection of the hidden depth of rock cracks by using a low-power microwave source and enhancing the amplitude of the transmission voltage. The method employs an active source mode and has conducted verification tests on cement mortar and granite samples with prefabricated cracks in the laboratory. The microwave frequency used in the study is 3.6 GHz, which enables real-time detection and has a rapid response speed, offering a new approach for the detection of crack depth in the field of rock engineering.

The measurement principle of hidden crack depth for rock

This paper presents a method for detecting the hidden crack depth in rock based on a microwave resonance model⁴⁴. Figure 1 shows the equivalent circuit diagram of the coupling relationship between the rock sample and the detection sensor. The detection method essentially utilizes the electromagnetic wave f_0 of the sensor to couple with the rock sample, causing the magnetic dipoles and electronic dipoles in the rock sample to resonate and generate a new resonance wave f_i . This wave energy propagates deep into the rock along the waveguide. When there is a crack in the rock sample, a reflecting surface is formed, which increases the characteristic impedance of the resonance wave, causing the resonance frequency f_0 to decrease and the wave amplitude to change, and increasing the energy consumption of the wave. Therefore, by using this microwave resonance model, the depth and distribution of hidden cracks in the rock sample can be predicted. It should be noted that different shapes of cracks and reflecting surfaces will cause different degrees of changes in wave energy consumption.

Specifically, the detection sensor is non-contact with the test piece. As shown in Fig. 1, U_s , R , and C_0 , are the equivalent output voltage of the microwave resonant oscillation signal, equivalent total resistance, and sensor capacitance, respectively. L_0 represents the sensor inductance, which is the key part of the microwave magnetic field. After L_0 generating resonance oscillation, the resonant oscillation frequency is expressed as f_0 , and its expression is Eq. (1).

$$f_0 = \frac{1}{2\pi} \sqrt{1/(L_0 C_0)} \quad (1)$$

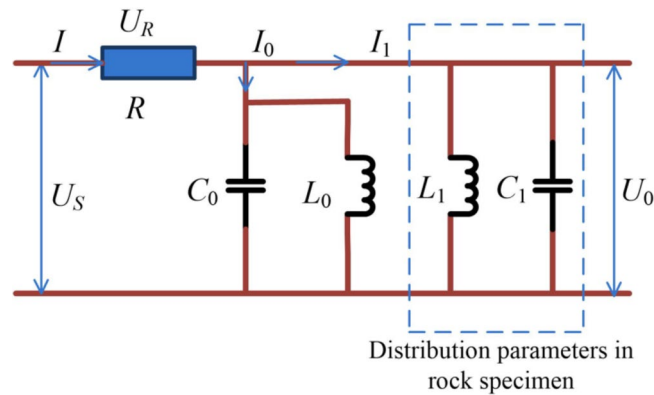


Fig. 1. Equivalent circuit schematic of sensor coupling with rock sample⁴⁴. U_S is the equivalent output voltage of the microwave resonance oscillation signal, R is equivalent total resistance, L_0 is the sum of the equivalent of sensor inductance and distribution parameter, and C_0 is the sum of the equivalent of the distribution parameters of sensor and resonance oscillation circuit capacitance, L_1 is distributed inductance after the tested sample is loaded, analogously, C_1 is distributed capacitance after the tested sample is loaded, and U_0 is resonance vibration output voltage. And I is total current, I_1 is load current, I_0 is no-load current, U_R is equivalent total resistance voltage.

In Fig. 1, L_1 and C_1 are the distributed inductance in the sample and distributed capacitance in the sample. When the sensor is coupled with the sample, L_1 and C_1 will resonate and produce an output voltage U_0 . The selected part in the dashed box indicates the distribution parameters in the rock sample to be tested.

By adjusting the distributed inductance L_1 and the distributed capacitance C_1 in the resonant oscillation network, the resonance vibration frequency f_l and output voltage U_0 can be changed to detect the depth of the hidden crack. The calculation of resonance vibration frequency f_l refers to Eq. (2).

$$f_l = \frac{1}{2\pi} \sqrt{\frac{1}{(L_0 + L_1)(C_0 + C_1)}} \quad (2)$$

Considering that excessively high frequencies are not conducive to computer sampling, we instead convert the frequency to voltage for analysis. According to Fig. 1, the resonant output voltage U_0 of the sensor can be obtained from the equivalent output voltage U_S of the microwave resonant signal and the equivalent total resistance voltage U_R , as detailed in Eq. (3).

$$U_0 = U_S - U_R \quad (3)$$

When the sensor is not coupled with the sample, it is called a no-load state; when the sensor is coupled with the sample, it is called a loaded state. In the no-load state, when the f_0 changes, the output voltage U_0 also changes correspondingly, and the change law can be observed in Fig. 2a; in the loaded state, change f_l , the output voltage U_0 also changes correspondingly, and the change law can be referred to Fig. 2b. The output voltage U_0 is increased by an order of magnitude compared with the published paper⁴⁴ of the author, as shown in Fig. 3. It's not difficult to find that there are differences in quantitatively detecting hidden crack depth and crack width using a microwave resonance model. In other words, quantitative detection of rock crack depth can be realized by using a low-power microwave source and enhancing the amplitude of emission voltage. Currently, the range of ultrasonic frequencies typically used for measuring the depth of cracks in cement mortar and rock is between 16 and 20 kHz, while the microwave frequency used in this study is 3.5–3.6 GHz. Compared to ultrasonic measurement methods, the advantage of microwave measurement is that it is 175,000 to 180,000 times faster in obtaining results for crack depth.

It is convenient and fast to evaluate the variation law of a hidden crack depth in rock based on the size of the output voltage U_0 . Figure 4 depicts the circuit diagram of the microwave resonance vibration detection system for assessing rock crack depth.

Experiment and analysis

Preparation of samples

The materials used in this experiment are commonly used granite and cement mortar, among which cement mortar is a typical material for simulating rock properties. The experimental samples were designed in a cuboid shape. Specifically, the granite sample was designed as a block piece with a “T” type crack, referred to as the “T” type crack sample, and labeled as T-X (X represents the serial number of the tested sample), as illustrated in Fig. 5a,c. The “T” type crack sample consists of three rectangular blocks denoted by A, B, and C. The dimensional parameters for each component are presented in Table 1. To meet the requirements of the study, all surfaces of the granite samples were polished to achieve an almost perfect mirror finish with a surface roughness of less than $\pm 5 \mu\text{m}$. The cement mortar test sample is labeled as C-X according to Fig. 5b,d. For this test, pre-cracked cement

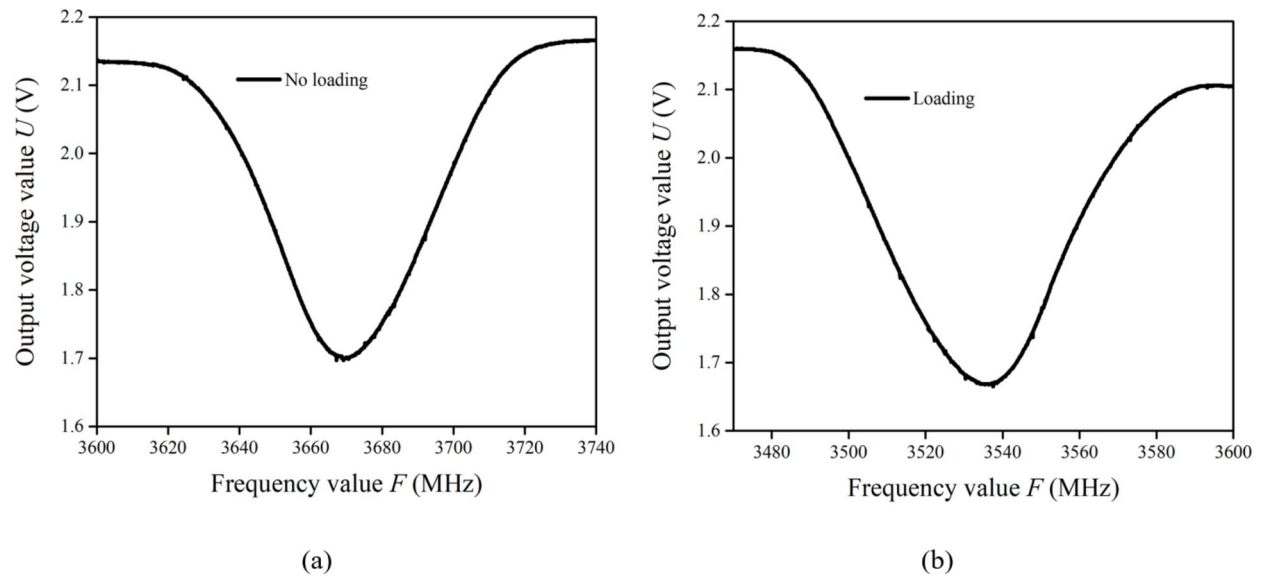


Fig. 2. Relationship curve between the output voltage and frequency of depth measuring apparatus: (a) no loading; (b) loading crack-free granite sample.

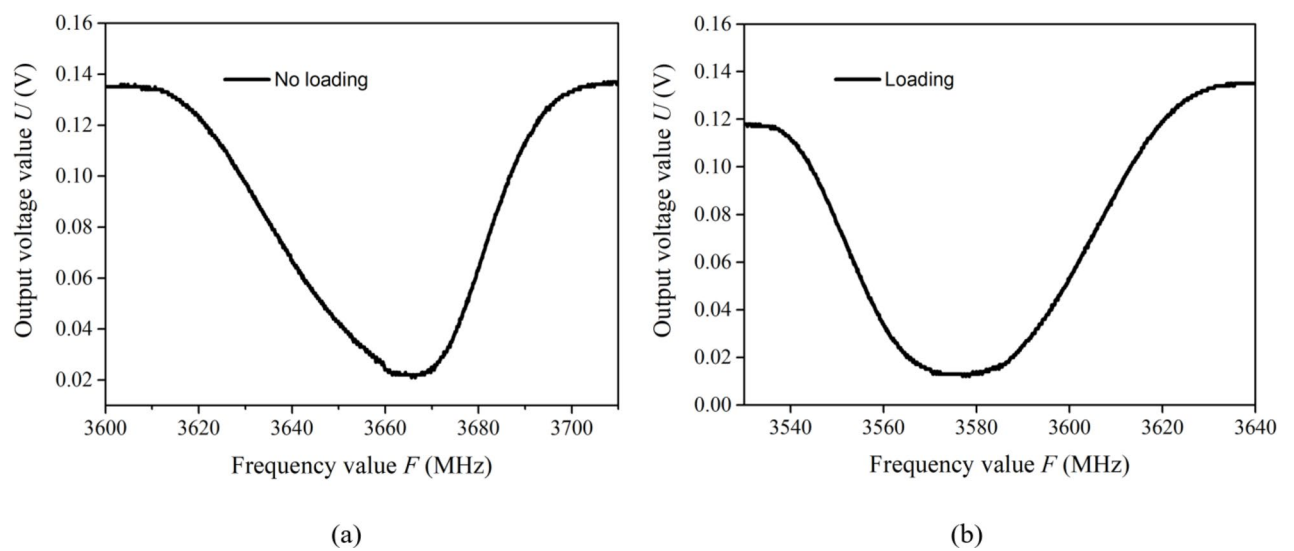


Fig. 3. Relationship curve between the output voltage and frequency of width measuring apparatus: (a) no loading; (b) loading crack-free granite sample⁴⁴.

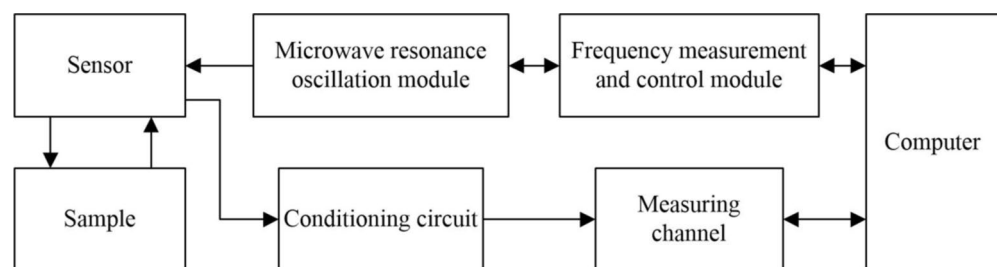


Fig. 4. Circuit block diagram of detecting system.

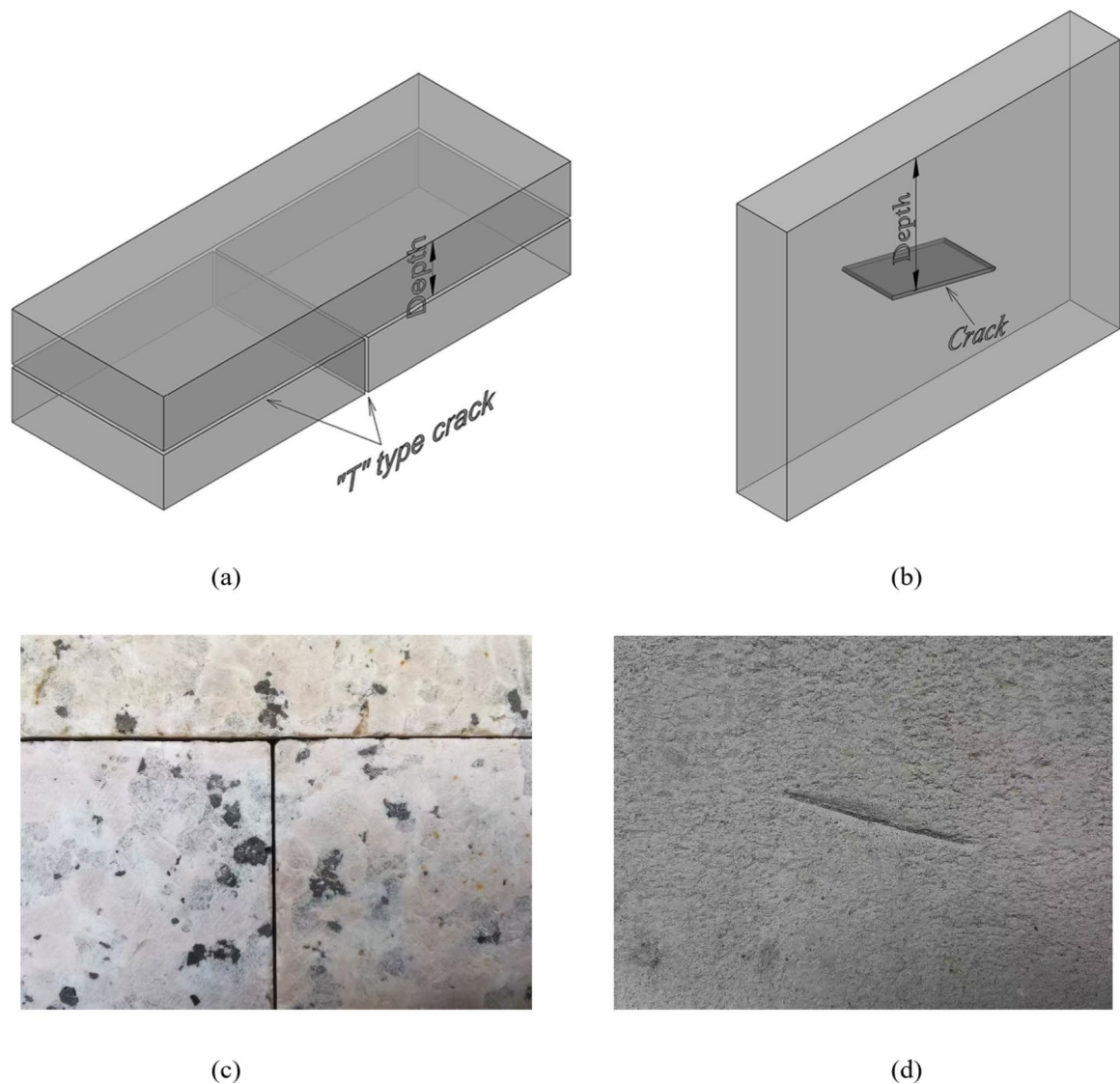


Fig. 5. Tested sample geometry: (a) “T” type crack sample (not-to-scale); (b) cement mortar sample (not-to-scale); (c) prefabricated cracks in “T” type crack sample; (d) prefabricated crack in cement mortar sample.

Sample composition	Length × width × height (mm)	Length × width × height (mm)	Length × width × height (mm)	Length × width × height (mm)
Part A	120 × 45 × 14	120 × 45 × 18	120 × 45 × 21	120 × 45 × 22
Part B	60 × 45 × 19	–	–	–
Part C	60 × 45 × 19	–	–	–

Table 1. Dimensional parameters of “T” type crack sample.

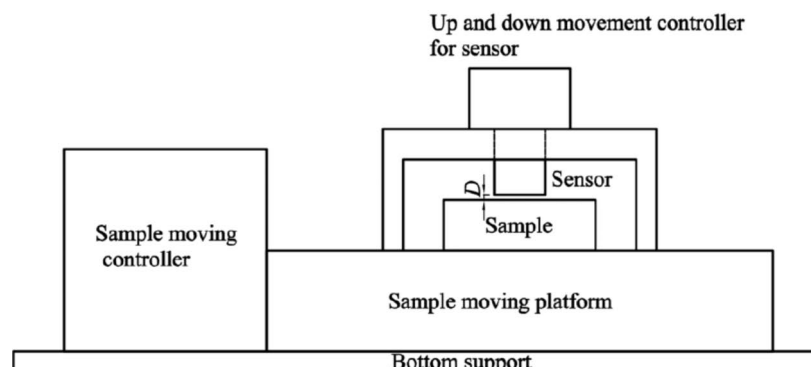
mortar samples made from white cement, river sand, and water at a ratio of 1:1:1 were used. The dimensions of the cement mortar sample are length × width × height = 200 mm × 30 mm × 150 mm. During the fabrication process, a plastic piece (with dimensions of length × width × thickness = 60 mm × 30 mm × 1.2 mm) should be precisely inserted at the center of the length and inclined at an angle of 15° from the horizontal direction to simulate a crack formation. Figure 5c,d respectively present the prefabricated cracks in the “T” type crack sample and the cement mortar sample. It is important to ensure even pouring of the cement mortar sample and thorough smoothing of its outer surface. Subsequently, the cement mortar samples were left to cure for 28 days. Considering the variations in rock mineralogy can affect the distribution of capacitance and inductance values, nuclear magnetic resonance (NMR) detection technology is used to screen the test samples, selecting those with relatively uniform material to be the test samples. It should be noted that the cracks in this sample are simulated cracks created in the laboratory.

Experimental procedure

The rock crack depth detection experiment was conducted on the rock hidden crack depth detection system shown in Fig. 6, where Fig. 6a is a photo of the measuring device, and Fig. 6b is a schematic diagram of the rock crack depth detection device's experimental platform. The test platform has dimensions of 290 mm length and 76 mm width and underwent precise machining to achieve mechanical runout within a 0.005 mm tolerance, while allowing for an axial maximum adjustable stroke of 125 mm. This platform provides controlled conditions for testing rock samples with different depths of prefabricated cracks. The hidden crack depth d is the vertical distance between the sample surface and the prefabricated crack. To assess the feasibility of the new method, a



(a)



(b)

Fig. 6. Rock hidden crack depth measurement device: (a) photo of the measuring device; (b) schematic diagram of the experimental platform for the rock crack depth detection device.

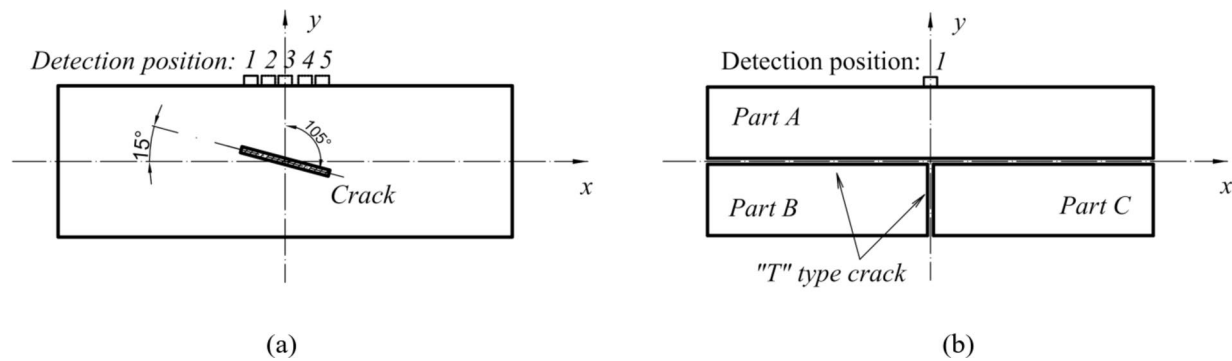


Fig. 7. Positions for sample detection: (a) cement mortar sample; (b) “T” type crack sample. In figure (a), “1”, “2”, “3”, “4”, and “5” correspond to the five inspection locations of the cement mortar sample; in figure (b), “1” corresponds to the inspection location of the “T” crack sample, which has only one inspection location.

Group	Sample nos.	Geometric size	Part A (mm)	Part B (mm)	Part C (mm)	Width-V (mm)	Width-H (mm)	Detection position no.	Hidden crack depth (mm)
Cement mortar sample	C-1	200×30×150	–	–	–	–	–	1	71
	C-2	200×30×150	–	–	–	–	–	2	72
	C-3	200×30×150	–	–	–	–	–	3	75
	C-4	200×30×150	–	–	–	–	–	4	79
	C-5	200×30×150	–	–	–	–	–	5	82
“T” type crack sample	T-6	120.005×45×33.005	14	19	19	0.005	0.005	–	14
	T-7	120.005×45×37.005	18	19	19	0.005	0.005	–	18
	T-8	120.005×45×40.005	21	19	19	0.005	0.005	–	21
	T-9	120.005×45×41.005	22	19	19	0.005	0.005	–	22

Table 2. Parameters of tested samples.

microwave signal source with a power supply of 5 V, a power of 50 mW, and a frequency of 15 GHz was used to ensure that the voltage resolution of the measurement system reached 3 μV, thereby improving the detection accuracy of cracks. Such design and parameter settings enable our system to effectively detect and distinguish cracks. The sensor for measuring the depth of the hidden crack in the rock is positioned directly above the test sample, maintaining a standoff distance *D* between the sensor and sample at 0.1 mm. Regarding the adjustment of the 0.1 mm gap between the sensor and the experimental sample, the sensor is capable of automatically adapting and adjusting the gap, thus no manual intervention is required during the experiment. The test sample was installed on the testing platform fixture, and the experiment began, with data being recorded, under ambient conditions of 27 °C temperature and 50% relative humidity. Therefore, a full testing process was carried out. The entire process, from sample clamping, data acquisition and processing, to the final result, takes approximately 30 s.

First, the crack depths of cement mortar samples were tested in this study. After installing the cement mortar sample on the test platform, the corresponding crack depths at detection positions 1, 2, 3, 4, and 5 were measured individually as depicted in Fig. 7a. The hidden crack depths at detection positions 1, 2, 3, 4, and 5 are 71 mm, 72 mm, 75 mm, 79 mm, and 82 mm, respectively.

Subsequently, to study the application of the microwave resonance vibration detection method to explore rock crack depth in real rock materials, a “T” type crack sample test was conducted on granite material. Specifically, hidden crack depth measurements were performed on “T” type crack samples labeled as T-6, T-7, T-8, and T-9 with corresponding depths set at 14 mm, 18 mm, 21 mm, and 22 mm respectively. During the experiment, portion A of the “T” type crack sample was modified to simulate varying depths of hidden cracks while keeping the slit width constant. In other words, both vertical (width-V) and horizontal (width-H) slit widths were fixed at 0.005 mm each. Throughout the test procedures, the sensor was positioned at the center of the “T” type crack, as shown in Fig. 7b.

In summary, the conducted experiments comprised two groups: the cement mortar tested sample (designated as C-X) test and the “T” type crack sample (designated as T-X) test. The detailed size parameters and quantities of the tested samples are presented in Table 2. A digital micrometer with a resolution power of 0.001 mm was employed as the scale during the experiment. To reduce the scatter of measurement data, each test for rock crack depth in the aforementioned experiment was repeated more than three times, and filtering measures were employed to suppress non-harmonic spurious signals to obtain the raw experimental data. Specifically, data

was collected 5 times at each measurement point, and then a five-point triple smoothing algorithm was used to process the data.

Results and analysis

Crack depth detection of cement mortar sample

The measurements of various hidden crack depths were conducted on cement mortar samples containing a pre-fabricated inclined crack. The testing procedure aimed to detect different hidden crack depths by changing the detection position of the same tested sample. The hidden crack depths for detection positions 1, 2, 3, 4, and 5 are respectively set as 71 mm, 72 mm, 75 mm, 79 mm, and 82 mm. The largest hidden crack depth corresponds to detection position 5, while the minimum hidden crack depth corresponds to detection position 1. The representative experimental results are shown in Fig. 8, where the raw data is not obtained in the form of time signals. This paper characterizes the depth of cracks based on changes in frequency and phase, and Fig. 8 illustrates the relationship curve between the output voltage value (U) of the measurement system and the resonance frequency (F). From Fig. 8 it can be observed that the amplitude of the output voltage signal from the measurement system is closely associated with hidden crack depth; as the hidden crack depth increases in the cement mortar sample, there is a decrease in output voltage from the detection system. It should be noted that as the crack depth increases, for example, if the hidden crack depth exceeds 82 mm, the ability of the sensor to detect crack depth decreases. The experimental conditions demonstrate the capability of the detection system to identify cement mortar samples containing hidden cracks with a maximum depth of 82 mm.

Crack depth detection of “T” type crack sample

To explore the practical use of the microwave resonance vibration detection method for determining the depth of cracks in real rock materials containing internal cracks, this section presents the experimental results from testing a sample with a “T” type crack. The representative experimental findings are shown in Fig. 9, which displays the relationship between the output voltage value (U) in volts and the resonant frequency (F) in megahertz of the measuring device. As depicted in Fig. 9, an increase in the depth of hidden cracks within the tested sample (ranging from 14 mm to 22 mm) results in a corresponding decrease in the amplitude of the output voltage detected by the system. These results show that the microwave resonance vibration detection method for rock crack depth can be effectively used for “T” type crack samples.

Evaluation model of rock crack depth

Based on the results of multiple experiments on samples with different materials and geometries, a significant amount of data was acquired to create a calibration model for detecting hidden crack depth. The experimental results (U - F curve) indicate that there is a clear correlation between the measured values of the hidden crack depth and the predetermined reference value of the hidden crack depth, and this relationship is nonlinear. The experiments show that the method of microwave resonance vibration detection can effectively detect hidden crack depths in cement mortar and granite samples. The concealed crack depth is denoted as “ d ”. According to the experimental results, the calibration model expression is shown in Eq. (4) below.

$$d = A_0 + A_1 e^{-x/A_2} \quad (4)$$

Where x represents U_0 ($0 < U_0 < 3.3$ V), the output voltage value of the sensor. Due to the different materials of the samples, the values of the coefficients in the formula should be different. The parameters A_0 , A_1 , and A_2 are closely related to the material's electrical conductivity, magnetic permeability, dielectric constant, and frequency

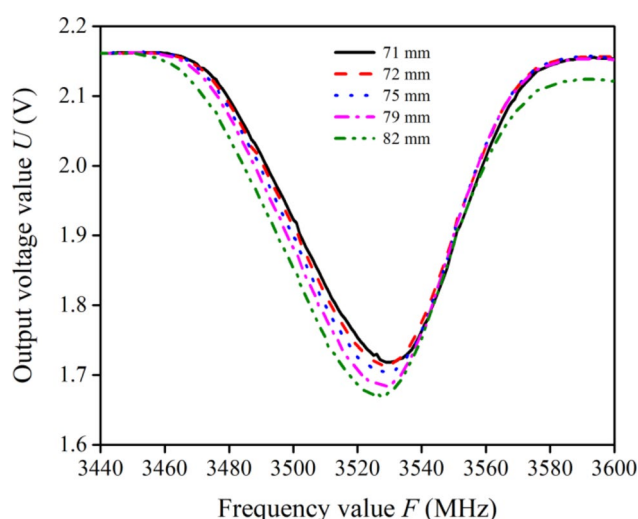


Fig. 8. Experimental results of the cement mortar sample. The figure illustrates the relationship between the output voltage of the measurement device and the resonant frequency.

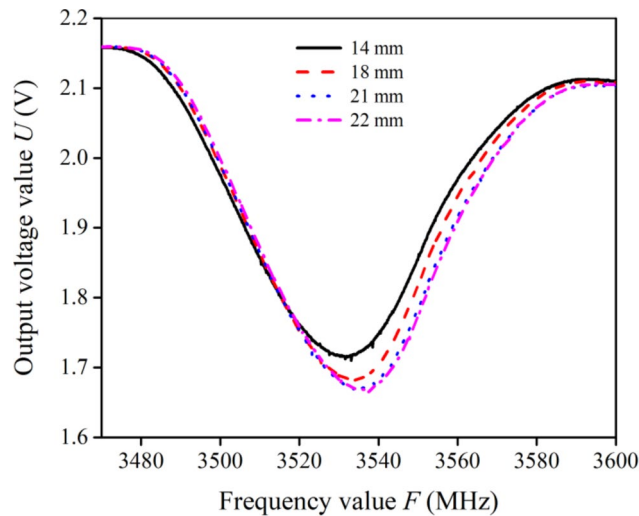


Fig. 9. Experimental results in “T” type crack sample. The figure illustrates the relationship between the output voltage of the measurement device and the resonant frequency.

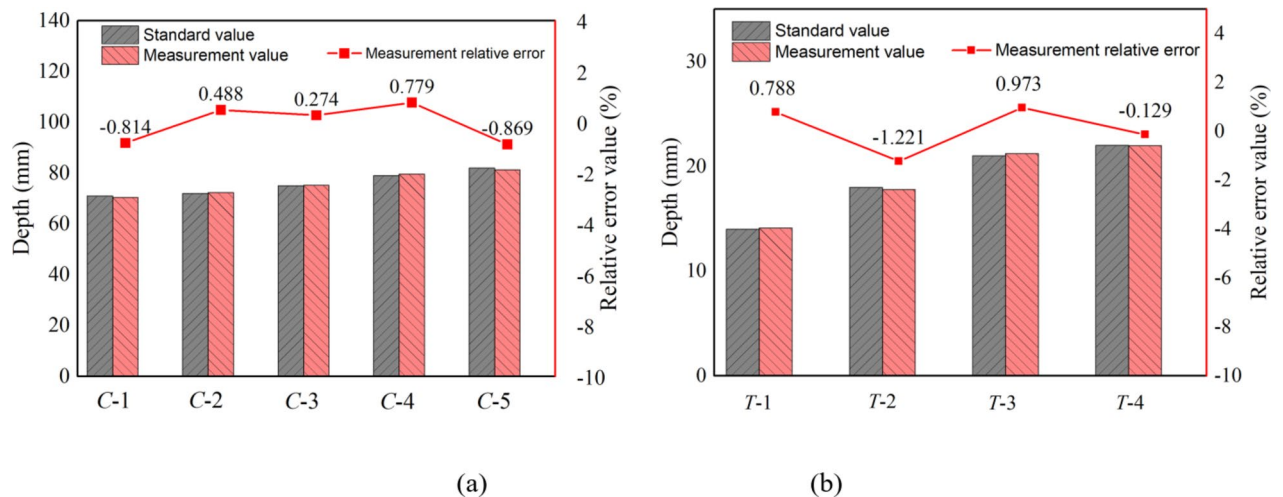


Fig. 10. Relative error between the actual measurement value and the standard value: (a) cement mortar sample; (b) “T” type crack sample..

characteristics. Specifically, for cement mortar samples, the coefficients are $A_0 = 85.050$, $A_1 = -1.144 \times 10^{-20}$, and $A_2 = -0.035$; whereas for granite samples, they are $A_0 = 12.846$, $A_1 = 5.212 \times 10^{32}$, and $A_2 = 0.023$. Furthermore, experimental results demonstrate that microwave propagation constant γ and reflection coefficient Γ differ across tested samples prepared with different materials.

Discussion

Hidden crack depth evaluation model for different geometries

According to the calibration model, the relative error between the measured value and the standard value (i.e., the preset reference value) of samples is depicted in Fig. 10. The samples include the cement mortar sample and the “T” type crack sample. It is evident from Fig. 10 that the measured values of the sample vary very little from the standard values. The maximum relative errors in the measurements of the cement mortar samples and the “T” type crack samples are -0.87% and -1.22% , respectively. In other words, the relative error of the measurement results is within $\pm 5\%$.

Analysis of propagation coefficient and reflection coefficient

Next, we theoretically analyze the microwave detection of hidden crack depth in rock materials through plane wave propagation. The objective of this subsection is to examine the propagation and reflection characteristics of the sample and assess the detectable range of crack depth. Radio waves propagating in free space do not cause reflection, refraction, scattering, absorption, and heat loss. The propagation of radio waves in free space was used

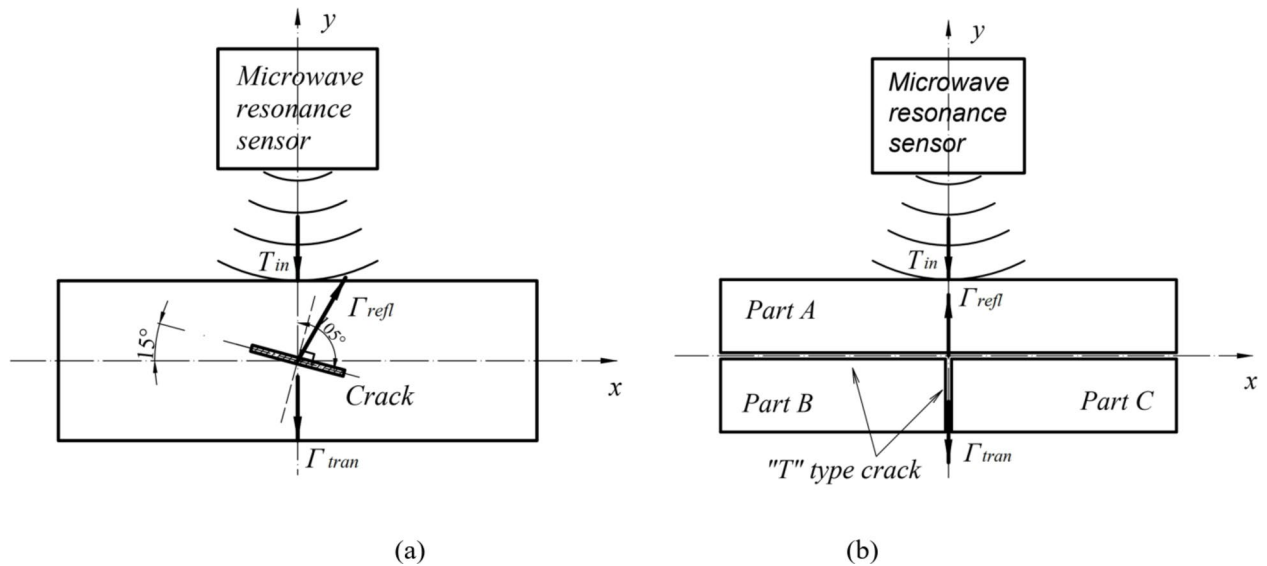


Fig. 11. Reflection and transmission in tested sample: (a) cement mortar sample; (b) “T” type crack sample (not-to-scale).

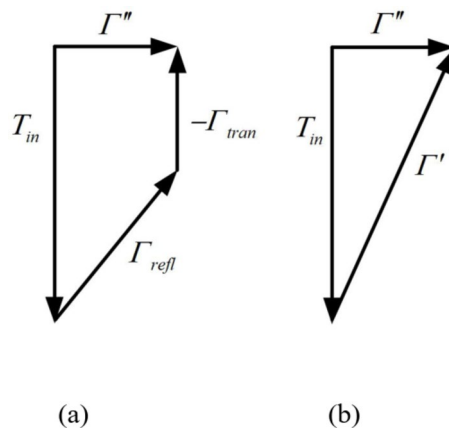


Fig. 12. Vector relationship between incident components.

as a reference for analyzing the actual propagation problems in this study. To simplify the analysis, absorption and heat loss are ignored here. The term “free space” refers to an area filled with a uniform ideal medium. Let the conductivity $\sigma = 0$, the permittivity $\varepsilon = \varepsilon_0$, the magnetic permeability $\mu = \mu_0$, and the permeability of vacuum $\mu_0 = 4\pi \times 10^{-7}$ (H/m). Upon irradiation of the microwave onto the smooth surface of the tested sample, a portion of the incident electromagnetic wave (T) was reflected, while another portion penetrated through to form transmission. The beam of electromagnetic wave undergoes variations in response to cracks within the sample, depending on their location and shape. The synthetic field strengths of the cement mortar sample and the granite sample are shown in Fig. 11. It can be observed from Fig. 11a that when an electromagnetic wave is incident upon a pre-cracked sample, it decomposes into several incident components. The depth and shape of a hidden crack can be detected by these incident components and phase differences. The prefabricated plexiglass sheet serving as the internal crack in Fig. 11a is extremely thin for the cement mortar sample. When subjected to electromagnetic waves, the crack behaves akin to air, resulting in a negligible reflected wave caused by it. The relationship between incident components of electromagnetic waves in cement mortar samples can be equivalently depicted in Fig. 12. According to Fig. 12, their vector relationships can be written as Eqs. (5) and (6).

$$\Gamma' = \Gamma_{refl} + \Gamma_{tran} \quad (5)$$

$$\Gamma'' = T_{in} - \Gamma' \quad (6)$$

Where Γ_{refl} represents the reflection component, Γ_{tran} denotes the transmission component, T_{in} signifies the incident wave field strength, Γ' is defined as the sum of the reflection component Γ_{refl} and the transmission

Name	Calculation formula	Granite material parameters	Calculated value of granite material G_1	Calculated value of granite material G_2	Cement mortar material parameters	Calculated value of cement mortar material C_1	Calculated value of cement mortar material C_2
Conductivity σ (S/m)		10^{-8} – 10^{-6}	10^{-8}	10^{-6}	10^{-3} – 10^{-2}	10^{-3}	10^{-2}
Permeability of vacuum μ_0 (H/m)	$\mu_0 = 4\pi \times 10^{-7}$	1.256×10^{-6}	1.256×10^{-6}	1.256×10^{-6}	1.256×10^{-6}	1.256×10^{-6}	1.256×10^{-6}
Relative permeability of sample μ_r	$\mu_r = \mu/\mu_0$	1.04	1.04	1.04	1.04	1.04	1.04
Magnetic permeability of sample μ (H/m)			1.306×10^{-6}	1.306×10^{-6}		1.306×10^{-6}	1.306×10^{-6}
Vacuum dielectric constant ϵ_0 (F/m)		8.854×10^{-12}	8.854×10^{-12}	8.854×10^{-12}	8.854×10^{-12}	8.854×10^{-12}	8.854×10^{-12}
Relative permittivity of sample ϵ_r	$\epsilon_r = \epsilon/\epsilon_0$	4–9	5	5	4–40	4	40
Permittivity of sample ϵ (F/m)			4.427×10^{-11}	4.427×10^{-11}		3.542×10^{-11}	3.542×10^{-10}
Angular frequency ω (Hz)	$\omega = 2\pi f$		2.217×10^{-10}	2.217×10^{-10}		2.217×10^{-10}	2.217×10^{-10}
Propagation constant γ	$\gamma = \sqrt{j\omega\mu\sigma}$		0.017	0.170		5.381	17.017
Wave impedance Z (Ω)	$Z = \frac{E}{H} = \frac{\gamma}{j\omega\epsilon} = \sqrt{j\omega\mu/\sigma}$		1.702×10^6	1.702×10^5		5.381×10^3	1.701×10^3
Wave impedance of sample Z_2 (Ω)	$Z_2 = \sqrt{\mu/\epsilon}$		171.772	171.772		192.047	60.731
Air dielectric wave impedance Z_1 (Ω)	$Z_1 = \sqrt{\mu_0/\epsilon_0}$		376.635	376.635		376.635	376.635
Reflection coefficient Γ	$\Gamma = \frac{Z_2 - Z_1}{Z_2 + Z_1}$		−0.374	−0.374		−0.325	−0.722
Microwave penetration depth d (mm)	$d = \sqrt{2/(\mu\omega\sigma)}$		83,107	8311		263	83

Table 3. Calculation examples of propagation constant γ , reflection coefficient Γ , and microwave penetration depth δ .

component \mathbf{T}_{tran} , and \mathbf{T}' is calculated as the difference between the incident wave field strength \mathbf{T}_{in} and the component \mathbf{T}' .

Similarly, for the granite samples, according to Fig. 11b, their vector relationship is given by Eq. (7).

$$\mathbf{T}_{in} = \mathbf{T}_{refl} + \mathbf{T}_{tran} \quad (7)$$

Where \mathbf{T}_{in} signifies the incident wave field strength, \mathbf{T}_{refl} represents the reflection component, and \mathbf{T}_{tran} denotes the transmission component.

The solution of each field quantity in Fig. 12 poses a significant challenge to obtain. In this regard, the value of the electric field strength E is acquired through experimental means, subsequently enabling the determination of hidden crack depth. Therefore, how can one ascertain the value of electric field strength E ? The method of calculating the electric field strength E is to obtain the changes of L_1 and C_1 in Fig. 1, with $U_0 = E$ also represented therein. It is also very difficult to measure or calculate the specific values of L_1 and C_1 . Therefore, it can only be solved by utilizing the changes between the resonance oscillation frequency f_0 and the resonance vibration frequency f_l of loading the tested sample. By considering the resonance oscillation angular frequency $\omega_0 = \sqrt{1/(L_0C_0)}$, we can derive the resonance vibration angular frequency $\omega_0' = \sqrt{1/(L'C')}$, which L' represents both the distributed inductance in the rock and the inductance of the resonance oscillation circuit ($L' = \frac{L_0 \times L_1}{L_0 + L_1}$) and C' denotes both the distributed capacitance in the rock and capacitance of the resonance oscillation circuit ($C' = C_1 + C_0$). Subsequently, taking a granite-tested sample as an example (Fig. 2), when coupling with a sensor, we observe a reduction in measured load frequency from 3.667 GHz (the no-load frequency) to 3.537 GHz. In other words, there is an incremental percentage change in angular frequency denoted by $\Delta\omega = (\omega_0 - \omega_0')/\omega_0 = 3.68\%$. After loading the tested sample, a reduction of 3.68% in resonance oscillation frequency is observed, attributed to the presence of distributed inductance L_1 and distributed capacitance C_1 . However, considering the small magnetic permeability of the granite sample, the contribution of inductance L_1 can be neglected. Therefore, it is evident that the primary factor influencing frequency change after sample loading is distributed capacitance C_1 . By measuring U_0 and phase difference, hidden crack depth within the tested sample can be determined.

After analyzing the microwave incidence of different samples, the maximum detection range of hidden crack depth is discussed herein. Under the experimental conditions outlined in this paper, we calculate the propagation constant and reflection coefficient of the tested sample. By examining the microwave component propagating to the surface of the sample, it can be observed that in the time domain, the electric field intensity vector E undergoes periodic changes when the frequency $f = \omega/(2\pi)$ varies. When conductivity σ , magnetic permeability μ , and dielectric constant are known, one can determine key parameters such as propagation constant γ , reflection coefficient Γ , and microwave penetration depth d for microwaves within a rock. The tested

cement mortar samples in this section exhibit a conductivity σ range of 10^{-3} to 10^{-2} S/m, a relative permeability μ_r of 1.04, a relative dielectric constant ε_r ranging from 4 to 40 F/m, and a resonance vibration frequency f_0 of 3.530 GHz. The corresponding calculation results are presented in Table 3. It can be observed from Table 3 that the propagation constant γ for cement mortar ranges from 5.381 to 17.017, the reflection coefficient Γ varies between -0.722 and -0.325 , and the penetration depth d within cement mortar spans from 83 to 263 mm.

Moreover, for granite sample, the conductivity of granite σ ranges from 10^{-8} to 10^{-6} S/m. The relative permeability μ_r of granite generally does not exceed 1.04, with a specific value of 1.04 adopted in this study. Additionally, the relative electric constant ε_r of granite is employed at 5 F/m and the resonance vibration frequency f_0 is determined as 3.530 GHz. The corresponding calculation results are presented in Table 3. The propagation constant γ of granite ranges from 0.017 to 0.170, as shown in Table 3. Additionally, the reflection coefficient Γ of granite is -0.374 , while the penetration depth d ranges from 8311 to 83,107 mm.

When the electromagnetic wave is coupled with the rock sample, due to its non-ideal reflectivity, a minimal reflection coefficient Γ is observed in the absence of a surface or internal crack. For cement mortar samples, the maximum measured depth of hidden crack was found to be 82 mm, which falls within the calculated microwave penetration depth range of 83 to 263 mm. Neglecting the influence of scattered electromagnetic waves, the crack depth measurement results align closely with theoretical calculations.

Currently, the range of sound wave frequencies typically used for ultrasonic measurement of crack depth in cement mortar and rock is between 16 and 20 kHz, while the microwave frequency used in this study is 3.5–3.6 GHz. Microwave measurement technology, compared to ultrasonic methods, has increased in speed by 175,000 to 180,000 times, and is theoretically capable of detecting rock cracks as deep as 83,000 mm, which is significantly greater than the detection depth of about 10,000 mm achieved by ultrasonic methods. However, in cement mortar, the depth of cracks measured by microwave is only 260 mm, which is less than the 500 mm depth that can be detected by the ultrasonic method. As the research progresses, we have found that the sensitivity of the measurement system is not only affected by the number of bits of the CPU but is also closely related to the width and depth of the cracks. The narrower and deeper the crack, the more difficult it is to identify. In addition, the interference in this detection method mainly comes from the discrete cavities within the rock and the electronic noise of the detection system. To ensure the accuracy of the research, we have excluded rock materials containing discrete cavities and obvious inhomogeneity. All rock materials and cement mortar samples used for experiments must pass nuclear magnetic resonance screening to confirm the absence of significant cavities before the experiment can proceed. Therefore, this paper primarily focuses on the impact of electronic noise in the detection system on the detection of crack depth, emphasizing the feasibility of the method and simplifying the treatment of complex issues.

Conclusions

This article introduces a rock crack depth detection technology based on the microwave resonance model. Under the premise of assuming material homogeneity, we tested the depth of hidden cracks in cement mortar and granite material samples. During the testing process, we coupled a 3.667 GHz microwave excitation signal to the samples to be tested and conducted a series of verification experiments to assess the effectiveness of the method. The analysis of the experimental results led us to the following conclusions:

- (1) The rock crack depth detection method based on the microwave resonance model can be used to measure the hidden crack depth of cement mortar material samples with preset oblique cracks and granite material samples with preset “T” cracks, confirming the feasibility of this method for detecting hidden crack depths.
- (2) Under experimental conditions, we found that the maximum detectable depth of hidden cracks in cement mortar samples can reach 82 mm, which matches the maximum depth of 82 mm calculated theoretically. For granite material samples, the maximum depth of hidden cracks calculated theoretically is 83,107 mm. As the depth of the cracks increases further, the sensitivity of the sensor will gradually decrease.
- (3) In this experiment, for the detection of rock crack depth, the maximum relative errors of the measurement results for cement mortar samples and granite samples are -0.869% and -1.221% , respectively, both of which are below the error range of $\pm 5\%$.

To enhance the practicality of the assessment model, the next focus of work will be to study the impact of discrete cavity distribution or non-homogeneous materials on the measurement of hidden crack depth. In addition, we will conduct experimental studies on hidden cracks in various rock materials such as sedimentary and metamorphic rocks, collecting depth detection data from these different types of rock materials to further enhance the practicality of the assessment model.

Data availability

The datasets used and/or analysed during the current study are available from the corresponding author on reasonable request.

Received: 21 June 2024; Accepted: 28 January 2025

Published online: 11 February 2025

References

1. Cheng, X., Qiao, W., He, H., Lusini, E. & Meng, X. Characteristics of regional geostress field and its impact on rock burst: a case study on the Binchang mining area, China. *Environ. Earth Sci.* **82**, 366. <https://doi.org/10.1007/s12665-023-11288-1> (2023).
2. Duan, Y. et al. Fracture fracture propagation and failure mode characteristics of lamellar lacustrine shale under true triaxial compression conditions. *Environ. Earth Sci.* **83**, 96. <https://doi.org/10.1007/s12665-023-11390-4> (2024).

3. Yu, L., Peng, K., Luo, S., Wang, Y. & Luo, K. Failure process and characteristics of deep concrete-supported arch tunnel under true-triaxial stress. *Theor. Appl. Fract. Mech.* **130**, 104295. <https://doi.org/10.1016/j.tafmec.2024.104295> (2024).
4. Zhang, J. et al. Study on crack propagation path of asphalt pavement under vehicle-road coupled vibration. *Appl. Math. Model.* **101**, 481–502. <https://doi.org/10.1016/j.apm.2021.09.004> (2022).
5. Du, K., Luo, X., Liu, M., Liu, X. & Zhou, J. Understanding the evolution mechanism and classification criteria of tensile-shear cracks in rock failure process from acoustic emission (AE) characteristics. *Eng. Fract. Mech.* **296**, 109864. <https://doi.org/10.1016/j.engfracmech.2024.109864> (2024).
6. Yong, Z. et al. Time-dependent behavior of reinforcement rock unit anchored by energy-absorbing bolt for large deformation control in tunneling. *Int. J. Rock. Mech. Min.* **174**, 105629. <https://doi.org/10.1016/j.ijrmm.2023.105629> (2024).
7. Li, J. et al. Study on the influence of perforation parameters on hydraulic fracture initiation and propagation based on CDEM. *Comput. Geotech.* **167**, 106061. <https://doi.org/10.1016/j.compgeo.2023.106061> (2024).
8. Wang, Y. & Lv, Z. Composite stimulation technology for improving fracture length and conductivity of unconventional reservoirs. *Front. Phys.* **11**, 1181302. <https://doi.org/10.3389/fphy.2023.1181302> (2023).
9. Yin, D. & Xu, Q. Comparison of sandstone damage measurements based on non-destructive testing. *Materials* **13**, 5154. <https://doi.org/10.3390/ma13225154> (2020).
10. Zhou, Z., Zheng, Y., Zhang, J. & Yang, H. Fast detection algorithm for cracks on tunnel linings based on deep semantic segmentation. *Front. Struct. Civ. Eng.* **17**, 732–744. <https://doi.org/10.1007/s11709-023-0965-y> (2023).
11. Guo, P. et al. Quantitative analysis of anisotropy effect on hydrofracturing efficiency and process in shale using X-ray computed tomography and acoustic emission. *Rock. Mech. Rock Eng.* **54**, 5715–5730. <https://doi.org/10.1007/s00603-021-02589-7> (2021).
12. Shi, D., Chen, X., Ning, Y., Bai, L. & Yu, X. Understanding the compression failure mechanism of rock-shotcrete composites using X-CT and DIC technologies. *Acta Geotech.* **18**, 5213–5230. <https://doi.org/10.1007/s11440-023-01884-7> (2023).
13. Wang, Y., Li, C. H. & Hu, Y. Z. X-ray computed tomography (CT) observations of crack damage evolution in soil-rock mixture during uniaxial deformation. *Arab. J. Geosci.* **11**, 199. <https://doi.org/10.1007/s12517-018-3561-z> (2018).
14. Li, L., Tan, Y., Huang, B. & Deng, X. Pore property as an indicator of macro-deterioration in slightly weathered tuffs. *Eng. Geol.* **267**, 105492. <https://doi.org/10.1016/j.enggeo.2020.105492> (2020).
15. Liu, T. et al. Nuclear magnetic resonance analysis of the failure and damage model of rock masses during freeze-thaw cycles. *Bull. Eng. Geol. Environ.* **81**, 445. <https://doi.org/10.1007/s10064-022-02944-0> (2022).
16. Ingraham, M. D., Issen, K. A. & Holcomb, D. J. Use of acoustic emissions to investigate localization in high-porosity sandstone subjected to true triaxial stresses. *Acta Geotech.* **8**, 645–663. <https://doi.org/10.1007/s11440-013-0275-y> (2013).
17. Niu, Y., Hu, Y. & Wang, J. Cracking characteristics and damage assessment of filled rocks using acoustic emission technology. *Int. J. Geomech.* **23**. <https://doi.org/10.1061/IJGNAL.GMENG-8034> (2023).
18. Wang, C. et al. Experimental investigation on the spatio-temporal-energy evolution pattern of limestone fracture using acoustic emission monitoring. *J. Appl. Geophys.* **206**, 104787. <https://doi.org/10.1016/j.jappgeo.2022.104787> (2022).
19. Liu, W. et al. Fracture precursor recognition and damage quantitative characterization of stressed rock using infrared radiation. *Rock. Mech. Rock. Eng.* **56**, 5567–5584. <https://doi.org/10.1007/s00603-023-03344-w> (2023).
20. Oswald-Tranta, B. Induction thermography for surface crack detection and depth determination. *Appl. Sci. Basel* **8**, 257. <https://doi.org/10.3390/app8020257> (2018).
21. Qiu, J., Pei, C., Liu, H. & Chen, Z. Quantitative evaluation of surface crack depth with laser spot thermography. *Int. J. Fatigue* **101**, 80–85. <https://doi.org/10.1016/j.ijfatigue.2017.02.027> (2017).
22. Arjun, V., Sasi, B., Rao, B. P. C., Mukhopadhyay, C. K. & Jayakumar, T. Optimisation of pulsed eddy current probe for detection of sub-surface defects in stainless steel plates. *Sens. Actuat. A-Phys.* **226**, 69–75. <https://doi.org/10.1016/j.sna.2015.02.018> (2015).
23. Jiang, F. & Liu, S. Evaluation of cracks with different hidden depths and shapes using surface magnetic field measurements based on semi-analytical modelling. *J. Phys. D Appl. Phys.* **51**, 125002. <https://doi.org/10.1088/1361-6463/aaef9> (2018).
24. Yang, L. et al. Uniform circular-array-based borehole pulsed eddy-current system for asymmetry defect inspection in downhole casings. *Electronics* **11**, 2030. <https://doi.org/10.3390/electronics11132030> (2022).
25. Yang, X. et al. Array waveguide probe loaded with split-ring resonators for sizing the cracks in metal surface. *IEEE Microw. Wirel. Co.* **28**, 171–173. <https://doi.org/10.1109/LMWC.2017.2788640> (2018).
26. Zhang, J. et al. Reliable crack monitoring based on guided wave through periodically loaded transmission line. *IEEE Sens. J.* **23**, 6799–6809. <https://doi.org/10.1109/JSEN.2023.3242672> (2023).
27. de Castro, D. L. & Bezerra, F. H. R. Characterization of a ghost-rock karst system controlled by fracture network and bedding planes in a semiarid region (NE Brazil) using ground penetrating radar (GPR). *Environ. Earth Sci.* **82**, 366. <https://doi.org/10.1007/s12665-023-11052-5> (2023).
28. Jin, Y. & Duan, Y. 2D wavelet decomposition and F-K migration for identifying fractured rock areas using ground penetrating radar. *Remote Sens. Basel.* **13**, 2280. <https://doi.org/10.3390/rs13122280> (2021).
29. Chang, C. W., Lin, C. H. & Yuan, Q. Quantitative study of electromagnetic wave characteristic values for mortar's crack. *Constr. Build. Mater.* **175**, 351–359. <https://doi.org/10.1016/j.conbuildmat.2017.09.171> (2018).
30. Koktavy, P. Experimental study of electromagnetic emission signals generated by crack generation in composite materials. *Meas. Sci. Technol.* **20**, 15704. <https://doi.org/10.1088/0957-0233/20/1/015704> (2009).
31. Salim, O., Dey, S., Masoumi, H. & Karmakar, N. C. Crack monitoring system for soft rock mining conveyor belt using UHF RFID sensors. *IEEE Trans. Instrum. Meas.* **70**, 8003412. <https://doi.org/10.1109/TIM.2021.3069025> (2021).
32. Song, D., Wang, E., Song, X., Jin, P. & Qiu, L. Changes in frequency of electromagnetic radiation from loaded coal rock. *Rock. Mech. Rock Eng.* **49**, 291–302. <https://doi.org/10.1007/s00603-015-0738-6> (2016).
33. Tian, X. et al. On the characterization and correlation of the rock failure-induced electromagnetic radiation and micro-vibration. *Eng. Geol.* **311**, 106879. <https://doi.org/10.1016/j.enggeo.2022.106879> (2022).
34. Guo, C. & Wu, S. Revealing crack initiation and extension of brittle rock via time-lapse acoustic attenuation: insights from active ultrasonic experiments. *Theor. Appl. Fract. Mech.* **132**, 104484. <https://doi.org/10.1016/j.tafmec.2024.104484> (2024).
35. Zhang, G. et al. Combined acoustic methods in monitoring the crack development in granite. *J. Appl. Phys.* **135**, 145104. <https://doi.org/10.1063/5.0200260> (2024).
36. Veltmeijer, A., Naderloo, M. & Barnhoorn, A. Precursors to rock failure in the laboratory using ultrasonic monitoring methods. *Geomech. Geophys. Geo.* **10**, 93. <https://doi.org/10.1007/s40948-024-00812-7> (2024).
37. Podymova, N. B., Ermolinskii, A. B. & Chernov, M. S. Nondestructive testing of local microcracking in laboratory mineral samples using an acoustic method with a laser source of ultrasound and its verification with X-ray computed tomography. *Russ. J. Nondestruct.* **59**, 1018–1026. <https://doi.org/10.1134/S1061830923600697> (2023).
38. Zhang, A. et al. Mechanical responses in rocks with different lithologies under mining loading-unloading: an insight by energy damage and ultrasonic characterization. *Rock Mech. Rock Eng.* <https://doi.org/10.1007/s00603-024-04081-4> (2024).
39. Zhang, T., Zhang, L., Ozevin, D. & Attard, T. Multi-scale ultrasonic imaging of sub-surface concrete defects. *Meas. Sci. Technol.* **35**, 35901. <https://doi.org/10.1088/1361-6501/ad128b> (2024).
40. Borges, D. et al. Experimental and theoretical analysis of finely bedded porous rock models with internal cracks. *Geophysics* **89**, T137–T149. <https://doi.org/10.1190/GEO2023-0160.1> (2024).
41. Zhou, Y. et al. Novel hard rock breaking technique using ultra-high-frequency particle impact induced by ultrasonic vibration field. *Energy* **288**, 129747. <https://doi.org/10.1016/j.energy.2023.129747> (2024).

42. Tao, M., Yang, Z., Zhao, Y., Wu, X. & Wu, C. Failure characteristics of microwave heat-treated stressed sandstone: implications for deep rock breakage using TBM cutting. *Energy* **292**, 130489. <https://doi.org/10.1016/j.energy.2024.130489> (2024).
43. Zhang, Y. et al. Influence of microwave irradiation and water-based cooling on the fracturing behavior and failure mode transition of CSTBD granite. *Eng. Fract. Mech.* **296**, 109832. <https://doi.org/10.1016/j.engfracmech.2023.109832> (2024).
44. Ou, C. et al. Quantitative detection of rock crack width using microwave resonance vibration eigenvalues. *IEEE Access* **7**, 49858–49871. <https://doi.org/10.1109/ACCESS.2019.2910538> (2019).

Acknowledgements

This research was supported by the Specific Research Project of Guangxi for Research Bases and Talents (NO. AD23026103); and the Middle-aged and Young Teachers' Basic Ability Promotion Project of Guangxi (NO. 2023KY0203). The author thanks the editors and reviewers for their efforts in improving the quality of the paper.

Author contributions

Conceptualization, Cj.O. and Y.C.; methodology, Cj.O. and B.M.; validation, Cj.O., Xd.Z. and Hc.C.; formal analysis, Xd.Z., Ct.O. and Hc.C.; investigation, Xd.Z., B.M. and Hc.C.; resources, Cj.O., Y.C. and Hc.C.

Declarations

Competing interests

The authors declare no competing interests.

Additional information

Correspondence and requests for materials should be addressed to B.M.

Reprints and permissions information is available at www.nature.com/reprints.

Publisher's note Springer Nature remains neutral with regard to jurisdictional claims in published maps and institutional affiliations.

Open Access This article is licensed under a Creative Commons Attribution-NonCommercial-NoDerivatives 4.0 International License, which permits any non-commercial use, sharing, distribution and reproduction in any medium or format, as long as you give appropriate credit to the original author(s) and the source, provide a link to the Creative Commons licence, and indicate if you modified the licensed material. You do not have permission under this licence to share adapted material derived from this article or parts of it. The images or other third party material in this article are included in the article's Creative Commons licence, unless indicated otherwise in a credit line to the material. If material is not included in the article's Creative Commons licence and your intended use is not permitted by statutory regulation or exceeds the permitted use, you will need to obtain permission directly from the copyright holder. To view a copy of this licence, visit <http://creativecommons.org/licenses/by-nc-nd/4.0/>.

© The Author(s) 2025